Carbide-derived carbons for dense and tunable 3D graphene networks

Carla de Tomas,[1, a)] Irene Suarez-Martinez,[1] and Nigel A. Marks[1]

Department of Physics and Astronomy, Curtin University, Perth WA 6102, Australia

The mechanical properties of carbide-derived carbons (CDCs) are computed using molecular dynamics simulations, spanning the experimental density range and synthesis temperatures. The structures consist of nanoporous networks with continuous graphene walls enclosing the pores. Calculation of elastic constants and simulation of tensile strain reveal a direct relationship between microstructure and elasticity, with density and temperature inducing significant changes in the pore topology and medium-range order. CDCs have a high elastic moduli and high ultimate tensile strengths while showing resistance to brittle fracture. This suggests that CDCs are a promising route to achieve dense 3D graphene networks with tunable mechanical properties.

The extremely high Young's modulus of graphene, of order 1 TPa, makes it an attractive starting point for the design of structures with outstanding mechanical properties. The challenge, however, is to create a carbon network which makes use of the excellent 2D mechanical properties of graphene while maintaining 3D connectivity. Using many different techniques (see Refs. 1 and 2 for a review), 3D graphene networks have been synthesized across a wide density range, from as little as 0.01 g/cc[3] to as high as 1.4 g/cc,[4] around 60% the density of graphite. Over this range the Young's modulus rises substantially, from 100 kPa up to 10 GPa, exhibiting a strong power-law dependence on density.[5] In this work we show that carbide-derived carbons (CDCs) are a promising addition to the family of 3D graphene networks. Using molecular dynamics simulations, we show that CDCs have excellent mechanical properties and significantly exceed the performance of equivalent density structures.

CDCs are nanoporous materials synthesized from a carbide precursor where the non-carbon atoms are removed via thermo-chemical treatments.[6] Typically this involves chlorination in combination with temperatures of 400–1200 °C. The density and porosity of CDCs are tunable via the choice of precursor and synthesis temperature and a wide number of precursor carbides have been studied.[6–11] As shown in Table I, CDCs have a density in the range 0.5–1.1 g/cc. The CDC literature is extensive and is dominated by the study of porosity and adsorption, as these properties enable numerous applications such as air and water filtering, energy storage and gas separation.[6,12–19] However, there are only a few experimental studies of CDCs from a mechanical point of view,[20–22] and we are not aware of any simulations of mechanical properties.

A variety of computational methods have been developed to produce CDC structures (see Ref. 23 for a review), ranging from simple geometric models[24] to sophisticated simulation-based techniques employing either monte-carlo atomistic reconstruction[25–29] or direct generation of coordinates by molecular dynamics.[30–35] Recently we generated TiC-CDC structures using an An-

nealed Molecular Dynamics (AMD) approach and found excellent agreement with experiments.[31] In a considerable improvement over previous studies, the AMD simulations predicted temperature-driven graphitization, radial distribution functions and absorption isotherms. A key component of the approach is using the transferable environment-dependent interaction potential (EDIP) for carbon,[36] which provides an excellent description of the competing hybridizations[37,38] and disordered carbon properties.[39,40]

In this Letter we compute the mechanical properties of CDCs with densities spanning the experimental range, and for each structure we determine the elastic constants and stress-strain curves. Figure 1 shows 14 structures created using our AMD approach. The CDC structures develop via long-time (3 ns) annealing of a face-centered-cubic lattice precursor with densities between 0.5 and 1.1 g/cc. To account for the effect of temperature on the microstructure each structure is annealed separately at low and high temperature. The simulation temperatures of $T_{low} = 2000$ K and $T_{high} = 4000$ K correspond approximately to experimental synthesis temperatures of 800 and 1200 °C, respectively, following an Arrhenius approach to bridge the large timescale gap between experiments and simulations.[31] Simulations are performed using LAMMPS,[41] with an NVE ensemble, a timestep of 0.2 fs and the Bussi thermostat. All structures contain 32,000 atoms and the atomic interactions are described using EDIP. A sensitivity analysis involving twenty 8,788-atom structures confirms that the results are statistically robust; see Supplementary Material for details.

Fig. 1 highlights the significant effect of temperature

a)Electronic mail: carladetomasandres@curtin.edu.au

TABLE I. Common carbide precursors and the corresponding carbide-derived carbon (CDC) density in g/cc. Density values calculated assuming a conformal transformation where the original shape and volume of the precursor is maintained.

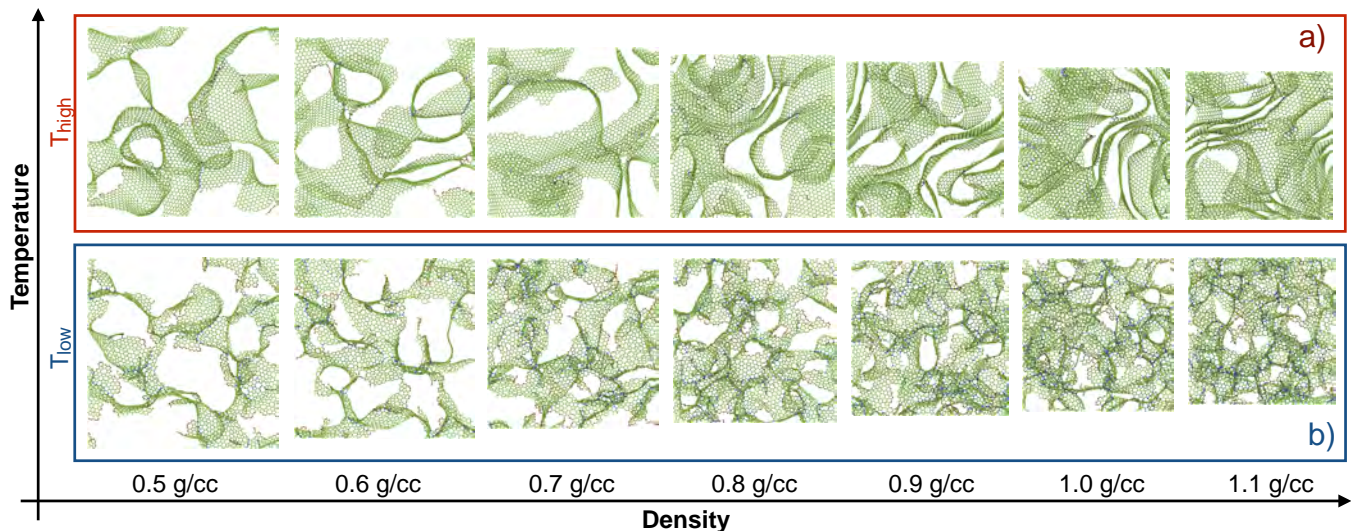| Ta$_2$C	Fe$_3$C	Ti$_3$AlC$_2$	Mo$_2$C	B$_4$C	Ti$_3$SiC$_2$	BaC$_2$
0.483	0.516	0.520	0.541	0.548	0.552	0.558
Al$_4$C$_3$	SrC$_2$	Ti$_2$AlC	ZrC	CaC$_4$	Cr$_3$C$_2$	NbC
0.591	0.686	0.733	0.783	0.832	0.891	0.895
TaC	WC	SiC	TiC	MoC	W$_2$C	VC
0.909	0.960	0.961	0.989	1.018	1.056	1.101

FIG. 1. Simulated CDC structures (2 nm cross-sections) obtained by annealing at, a) T_{high}, and b) T_{low}. Red, green and blue spheres denote sp, sp^2 and sp^3 bonded atoms, respectively. All structures contain 32,000 atoms, and box lengths decrease from 10.9 nm (0.5 g/cc) to 8.3 nm (1.1 g/cc).

and density on CDCs. While all the structures are highly sp^2-bonded, temperature drives significant differences in their microstructures. At T_{low}, all the structures remain disordered, featuring small and convoluted graphene platelets often linked to each other by sp^3 bonds. When the density increases, the pores become smaller and there are more links among platelets. At T_{high}, all the structures become more ordered, with large, planar graphene platelets seen at low density. As the density increases, graphene layers start to stack, giving rise to small graphitic domains. For the highest density of 1.1 g/cc, we observe up to four stacked layers as shown in the right-most image in Fig. 1(a). The transition from highly disordered carbon to stacked layers is well known experimentally,[8,42,43] and the close correspondence between simulation and experiments is extensively discussed for the specific case of TiC-CDCs (density of 0.98 g/cc) in Ref. 31.

To quantify the degree of order and graphitization, coordination fractions and ring statistics are computed for all structures (full details in supplementary material). For the T_{high} structures the sp, sp^2 and sp^3 fractions are independent of density, with mean values of 1.4%, 98% and 0.6%, respectively. The small percentage of sp atoms indicates that the structures are continuous 3D networks, since sp atoms occur primarily at the edges of graphene platelets. In addition, the low sp^3 fraction indicates that cross-linking between graphene fragments is minimal. At T_{low} the sp^2 fraction decreases linearly from 90% at 0.5 g/cc to 84% at 1.1 g/cc, while the sp^3 fraction increases by a similar amount (from 4% to 10%) over the same range. This indicates considerable amounts of cross-linking between small graphene fragments, creating small pores. Ring statistics characterize the topology of the network and reveal no density dependence. The

T_{high} structures are dominated by hexagons, typical of graphene, while the T_{low} structures contain appreciable numbers of pentagons and heptagons, with excess of the former. This excess produces positive curvature which encloses the pores, as seen in Fig. 1(b).

For each of the structures in Fig. 1 we compute the elastic constant tensor C_{ij} by finite difference (see supplementary material for details). Each element of the elastic constant tensor C_{ij} is calculated as the ratio between the stress and the strain in the corresponding direction. For the T_{low} structures the elements C_{ij} have the symmetry of a cubic material and can be characterized by the principal elastic constants C_{11}, C_{12}, and C_{44}. Consistent with visual inspection of Fig. 1(a), the C_{ij} for the T_{high} structures exhibit some anisotropy. However, this is a consequence of the finite size of our simulations and the relatively small number of domains.

Using the elastic constants and the Hill formulae [Eqs. (S1)-(S9) in supplementary material] we determine the bulk modulus, shear modulus, Young's modulus and Poisson's ratio. As shown in Fig. 2, the moduli vary strongly with density and temperature. For example, the bulk and shear moduli for the T_{low} structures increase by nearly a factor of six over the range 0.5 to 1.1 g/cc. The T_{high} structures also exhibit a significant increase, varying by a factor of three to four. This tunability shows how CDCs can be selected for a particular mechanical application by the appropriate choice of carbide precursor and synthesis temperature.

The sensitivity of the elastic properties to density and temperature reflects the spectrum of CDC microstructures. At low densities the moduli values are similar at both temperatures, while large differences occur at high densities due to the stacked graphene layers. These graphitic domains can be compressed by narrowing the
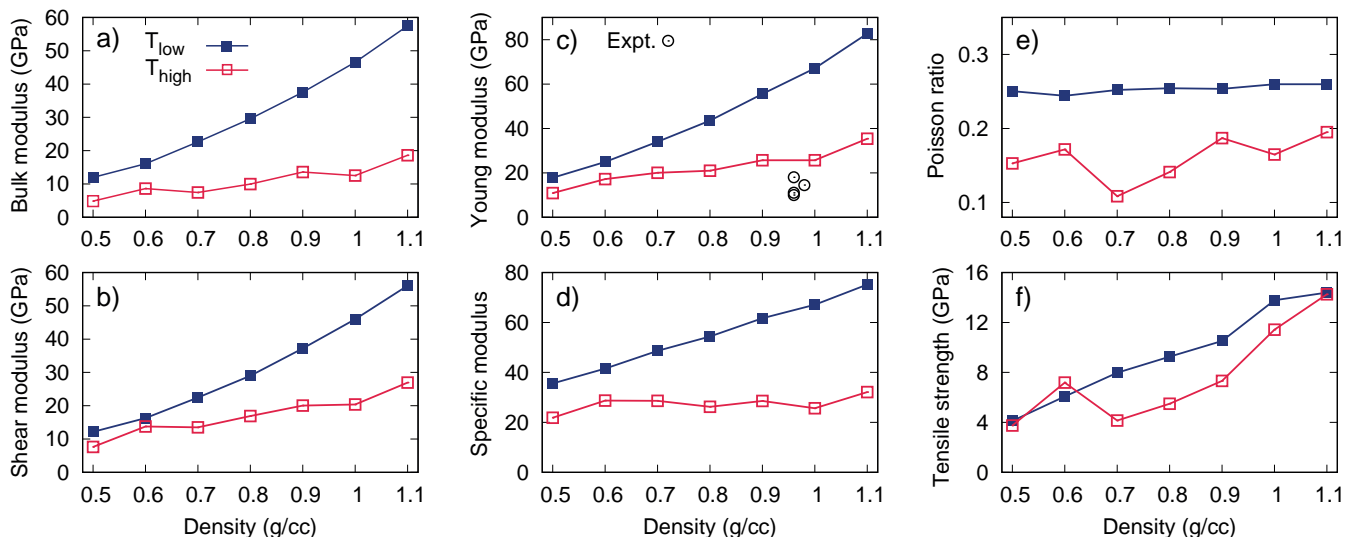
FIG. 2. Density and temperature variation of a) bulk modulus, b) shear modulus, c) Young's modulus (averaged across the Cartesian directions), d) specific modulus, in units of GPa/(g/cc), e) Poisson's ratio and f) ultimate tensile strength. Experimental values of the Young's modulus for SiC-CDC and TiC-CDC[20,21,44] are shown as black circles in panel c).

FIG. 3. Stress-strain curve for the 1.0 g/cc CDC annealed at T_{high}. Snapshots of a 1.5 nm depth slab along the x-axis are shown at key stages: a) initial configuration, b) elastic regime, c) ultimate tensile stress point, d) small fractures during plastic regime, and e) superplastic regime. Color code as in Fig. 1.

interlayer distance, while the pore walls in the microporous structures at T_{low} provide resistance to deformation. The microstructural differences similarly explain the difference in shear moduli as the graphene layers can slide over each other. Figure 2 shows that Poisson's ratio for the T_{low} structures is roughly constant and equal to 0.25, as expected for an isotropic material. Due to the anisotropy and system-size effects, values for T_{high} structures fluctuate between 0.11 and 0.20, similar to ex-

perimental values of 0.165–0.19 reported for graphite.[45]

The stiffness of a material is characterized by its Young's modulus and is a key quantity in engineering applications. Often called simply the elastic modulus, the Young's modulus [Fig. 2(c)] varies significantly with density, changing by a factor of four for both temperatures. The black circles in the figure show experimental data of CDCs in various forms (thin films[20,44] and monoliths/bulk[21]) synthesized from SiC and TiC precursors. The experimental values are clustered in the range 8–18 GPa and compare well with the computed elastic constants for the T_{high} structures, confirming that our methodology is realistic. Dividing the Young's modulus by the density yields the specific modulus, an important materials property used to design structures where minimum weight is required, such as airplanes, masts and bicycle frames. CDCs have a specific modulus [Fig. 2(d)] in the range 20–80 GPa/(g/cc), superior to common light metals such as aluminum, titanium and magnesium that all have a specific modulus around 25 GPa/(g/cc).

Tensile stress-strain curves are computed for each CDC structure by imposing a uniaxial strain along the x-axis. A strain rate of 0.001 ps^{-1} is applied to the system every 0.02 ps. The simulation runs for 2 ns in the NPT ensemble using a Nosé-Hoover thermostat/barostat to keep the temperature at 300 K and the pressure at zero in y- and z-directions; the barostat ensures that the system responds dynamically to the applied strain. Figure 3 shows a stress-strain curve for a T_{high} structure at 1.0 g/cc, with key stages indicated by the snapshots. The structure can withstand significant strain (nearly 0.20) in the linear, or elastic, regime [Fig. 3(b)], indicating that CDCs are quite ductile. Beyond the yield strain, the structure undergoes plastic deformation, attaining a maximum tensile strength [Fig. 3(c)]. Past this point, the
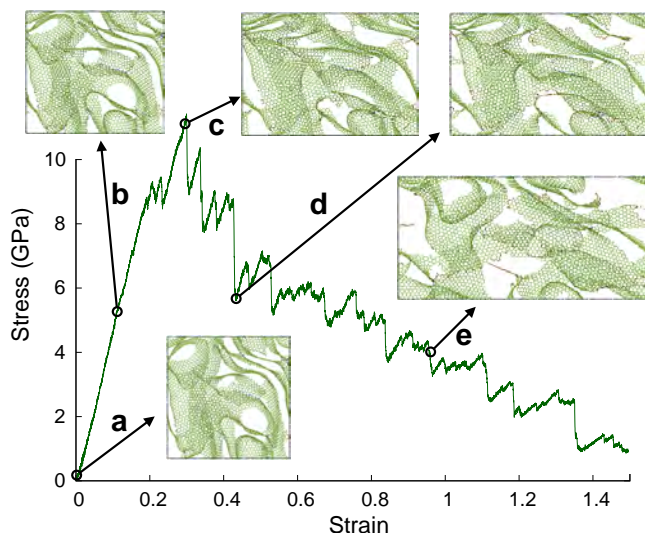
TABLE II. Variation of yield stress (units of GPa) and yield strain with density and temperature. Values obtained by visual inspection of the stress-strain curve for each structure.

Density (g/cc)		0.5	0.6	0.7	0.8	0.9	1.0	1.1
Yield stress	T_{high}	3.4	4.7	2.8	4.6	6.5	8.8	13.0
	T_{low}	3.3	5.0	6.8	7.9	9.2	12.6	12.9
Yield strain	T_{high}	0.22	0.19	0.22	0.23	0.17	0.19	0.16
	T_{low}	0.15	0.13	0.15	0.17	0.16	0.16	0.15

FIG. 4. Relationship between Young's modulus and density for a variety of sp^2-bonded carbon materials. Data for CDCs (this work), is shown with triangles. All other data is extracted from Fig. 4 in Ref. 5. The solid line is a fitted power-law relationship from Ref. 5.

structure begins to fracture, but unlike many materials, the fracture process is gradual rather than abrupt. During fracture, short filaments of sp-bonded atoms form, see red atoms in Fig. 3(d), and these increase in length with strain. This behavior, which resembles superplasticity, allows the structure to maintain a significant tensile stress, even when it expands to nearly twice its original volume [Fig. 3(e)].

Figure 2(f) shows the density and temperature dependence of the ultimate tensile strength determined from the point of maximum stress in the stress-strain curves. While the ultimate strength varies strongly with density, the temperature only has a minor effect. Even for the lowest density CDCs, the ultimate tensile strength is significantly higher than common light metals and alloys, such as titanium (0.79 GPa), stainless steel (0.95 GPa)[46] and aluminium alloys (0.48 GPa),[47] and also higher than heavy metals, such as tungsten (1.51 GPa). The yield stress and yield strain are obtained from the last point in the linear regime (see Table II). Again, the density has the strongest influence on properties, while temperature plays a minor role: the mean yield strain for T_{high} structures is 0.20, and 0.15 for T_{low}. The slope of the elastic region of the stress-strain curves provide an alternate route to compute the Young's modulus. As shown in the supplementary material, there is good correlation with the values from the elastic constant tensor, with the two approaches having an average difference of $\sim$20% for T_{high} and $\sim$10% for T_{low} structures.

Worsley et al.[5] collected data for 3D graphene networks for various synthesis methods (carbon aerogels, carbon nanotube assembly, and graphene assemblies obtained via three different routes: freeze-drying of hydrogel precursors, gelation of graphene oxide and 3D printing) and found that the Young's modulus follows a power-law dependence on density with an exponent of 2.7. Figure 4 plots their data, along with our CDC structures; for reference, also shown is single sheet graphene and commercial graphite. As seen from the Figure, most efforts to synthesize 3D graphene networks have focussed on low-density structures; CDCs not only provide a convenient route for creating high-density 3D graphene networks, they also outperform the trend line. An explanation for this behaviour could be that the computed CDC structures are fully 3D connected and have low heterogeneity. The relatively high density of CDCs opens the possibility of biomedical implant applications where materials
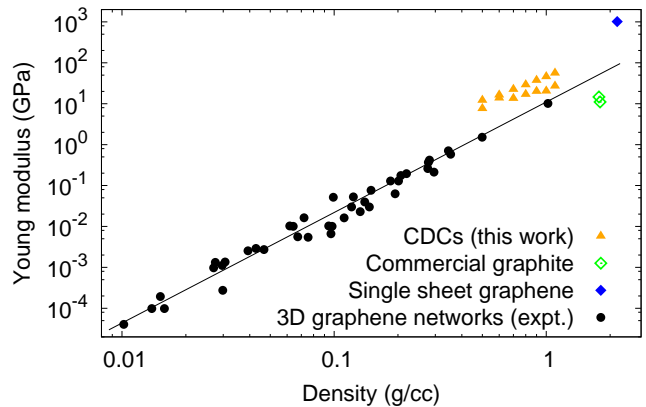
with a Young's modulus similar to bone are desirable. Human bone has a modulus in the range 10–30 GPa, while common implant metals such as stainless steel, titanium and CoCr alloys have much higher moduli, in the range 100–200 GPa. This elasticity mismatch leads to bone-resorption and loosening of the implant, a problem known as stress-shielding.[46,48,49]

The challenge in applying CDCs for structural applications concerns the synthesis route, in particular kinetics associated with infiltration of the chlorine etchant. Presently, the highest quality CDCs are prepared as powders or thin films, with typical processing times of several hours. The difficulty comes with monolithic/bulk CDCs, where slow kinetics can become prohibitive. Several groups[21,50–52] have developed hierarchical approaches to accelerate the kinetics substantially (by up to 100x) but from a mechanical point-of-view, the downside is that the structure varies across length scales. Such materials do not respond uniformly to mechanical deformation; e.g. Fey et al.[21] synthesized hierarchical SiC-CDC and reported a Young's modulus of 10 GPa but the compressive strength was 5000 times smaller, at around 2 MPa.

Although this work focusses on CDCs, it is possible that other synthesis routes might yield similar carbon nanostructures with comparable properties. For example, carbon nanomembranes fabricated by irradiation of self-assembled-monolayers have a Young's modulus of 10–20 GPa, increasing up to 50 GPa after annealing.[53] Recent simulations[54] of self-assembly of graphene flakes also produced 3D graphene networks broadly similar to our CDCs at T_{low}. Although a different potential was used and the density and the Young's modulus were lower than our work, 0.36 g/cc and 2.8 GPa, respectively, similar superplastic behavior was observed.

In summary, we propose carbide-derived carbons (CDCs) as a potential pathway to create dense 3D graphene networks. The calculations reproduce the lim-

ited experimental data available, and demonstrate that CDCs have potential as a structural material. Despite having a density much lower than metals, CDCs are ductile and have an excellent ultimate tensile strength. We find that the elastic moduli vary significantly with density and synthesis temperature, indicating that CDCs can also be tuned for particular mechanical applications. These characteristics arise from the CDC microstructure which consists of graphene-like fragments enclosing nanometre-sized pores. Given the potential merit of CDCs as a route towards 3D graphene networks, we hope this work stimulates experimental interest in fabricating non-hierarchical, monolithic CDCs and characterizing their mechanical properties.

See Suppl. Mat. for details on the sensitivity analysis, microstructure characterization, calculation of the mechanical properties and stress-strain curves for all the structures.

[1] Q. Fang, Y. Shen, and B. Chen, Chem. Eng. J. **264**, 753 (2015).

[2] W. Lv, C. Zhang, Z. Li, and Q. H. Yang, J. Phys. Chem. Lett. **6**, 658 (2015).

[3] Y. Qin, Q. Peng, Y. Ding, Z. Lin, C. Wang, Y. Li, F. Xu, J. Li, Y. Yuan, X. He, and Y. Li, ACS Nano **9**, 8933 (2015).

[4] X. Han, Z. Yang, B. Zhao, S. Zhu, L. Zhou, J. Dai, J.-W. Kim, B. Liu, J. W. Connell, T. Li, B. Yang, Y. Lin, and L. Hu, ACS Nano **11**, 3189 (2017).

[5] M. A. Worsley, S. Charnvanichborikarn, E. Montalvo, S. J. Shin, E. D. Tylski, J. P. Lewicki, A. J. Nelson, J. H. Satcher, J. Biener, T. F. Baumann, and S. O. Kucheyev, Adv. Func. Mater. **24**, 4259 (2014).

[6] V. Presser, M. Heon, and Y. Gogotsi, Adv. Funct. Mater. **21**, 810 (2011).

[7] A. M. Kern, B. Zierath, J. Haertlé, T. Fey, and B. J. M. Etzold, Chem. Eng. Technol. **39**, 1121 (2016).

[8] A. C. Forse, C. Merlet, P. K. Allan, E. K. Humphreys, J. M. Griffin, M. Aslan, M. Zeiger, V. Presser, Y. Gogotsi, and C. P. Grey, Chem. Mater. **27**, 6848 (2015).

[9] A. Jänes, T. Thomberg, and E. Lust, Carbon **45**, 2717 (2007).

[10] G. N. Yushin, E. N. Hoffman, A. Nikitin, H. Ye, M. W. Barsoum, and Y. Gogotsi, Carbon **43**, 2075 (2005).

[11] R. K. Dash, G. Yushin, and Y. Gogotsi, Microporous Mesoporous Mat. **86**, 50 (2005).

[12] Z. Kou, B. Guo, Y. Zhao, S. Huang, T. Meng, J. Zhang, W. Li, I. S. Amiinu, Z. Pu, M. Wang, M. Jiang, X. Liu, Y. Tang, and S. Mu, ACS Appl. Mater. Interfaces **9**, 3702 (2017).

[13] W. Li, Y. Li, Y. Chen, Q. Liu, Y. Lu, H. Meng, and C. Li, Energy Fuels **31**, 9035 (2017).

[14] M. Oschatz, S. Boukhalfa, W. Nickel, J. P. Hofmann, C. Fischer, G. Yushin, and S. Kaskel, Carbon **113**, 283 (2017).

[15] S. Schweizer, R. Meissner, M. Amkreutz, K. Thiel, P. Schiffels, J. Landwehr, B. J. M. Etzold, and J.-R. Hill, J. Phys. Chem. C **121**, 7221 (2017).

[16] J. Chmiola, C. Largeot, P.-L. Taberna, P. Simon, and Y. Gogotsi, Science **328**, 480 (2010).

[17] Y. Korenblit, M. Rose, E. Kockrick, L. Borchardt, A. Kvit, S. Kaskel, and G. Yushin, ACS Nano **4**, 1337 (2010).

[18] Y. Gogotsi, A. Nikitin, H. Ye, W. Zhou, J. E. Fischer, B. Yi, H. C. Foley, and M. W. Barsoum, Nature Mater. **2**, 591 (2003).

[19] T. J. Bandosz, M. J. Biggs, K. E. Gubbins, Y. Hattori, T. Iiyama, K. Kaneko, J. Pikunic, and K. T. Thomson, *Chemistry and physics of carbon*, Vol. 28 (Marcel Dekker, New York, 2003).

[20] P. Huang, C. Lethien, S. Pinaud, K. Brousse, R. Laloo, V. Turq, M. Respaud, A. Demortière, B. Daffos, P. L. Taberna, B. Chaudret, Y. Gogotsi, and P. Simon, Science **351**, 691 (2016).

[21] T. Fey, B. Zierath, A. M. Kern, P. Greil, and B. J. M. Etzold, Carbon **70**, 30 (2014).

[22] J. Torop, V. Palmre, M. Arulepp, T. Sugino, K. Asaka, and A. Aabloo, Carbon **49**, 3113 (2011).

[23] S. K. Bhatia, Langmuir **33**, 831 (2017).

[24] Q. Cai, A. Buts, M. J. Biggs, and N. A. Seaton, Langmuir **23**, 8430 (2007).

[25] A. H. Farmahini, G. Opletal, and S. K. Bhatia, J. Phys. Chem. C **117**, 14081 (2013).

[26] P. Kowalczyk, A. P. Terzyk, P. A. Gauden, S. Furmaniak, M. Wisniewski, A. Burian, L. Hawelek, K. Kaneko, and A. V. Neimark, J. Phys. Chem. C **118**, 12996 (2014).

[27] T. X. Nguyen, S. K. Bhatia, S. K. Jain, and K. E. Gubbins, Mol. Sim. **32**, 567 (2007).

[28] S. K. Jain, R. J. M. Pellenq, J. P. Pikunic, and K. E. Gubbins, Langmuir **22**, 9942 (2006).

[29] G. Opletal, T. C. Petersen, D. G. McCulloch, I. K. Snook, and I. Yarovsky, J. Phys.: Condens. Matter **17**, 2605 (2005).

[30] M. W. Thompson, B. Dyatkin, H.-W. Wang, C. H. Turner, X. Sang, R. R. Unocic, C. R. Iacovella, Y. Gogotsi, A. C. T. van Duin, and P. T. Cummings, C **3** (2017), 10.3390/c3040032.

[31] C. de Tomas, I. Suarez-Martinez, F. Vallejos-Burgos, M. J. Lopez, K. Kaneko, and N. A. Marks, Carbon **119**, 1 (2017).

[32] R. Ranganathan, S. Rokkam, T. Desai, and P. Keblinski, Carbon **113**, 87 (2017).

[33] L. J. Peng and J. R. Morris, Carbon **50**, 1394 (2012).

[34] M. J. López, I. Cabria, and J. A. Alonso, J. Chem. Phys. **135**, 104706 (2011).

[35] J. C. Palmer, A. Llobet, S. H. Yeon, J. E. Fischer, Y. Shi, Y. Gogotsi, and K. E. Gubbins, Carbon **48**, 1116 (2010).

[36] N. A. Marks, Phys. Rev. B **63**, 035401 (2000).

[37] C. de Tomas, I. Suarez-Martinez, and N. A. Marks, Carbon **109**, 681 (2016).

[38] R. C. Powles, N. A. Marks, D. W. M. Lau, D. G. McCulloch, and D. R. McKenzie, Carbon **63**, 416 (2013).

[39] I. Suarez-Martinez and N. A. Marks, Appl. Phys. Lett. **99**, 033101 (2011).

[40] T. B. Shiell, D. McCulloch, D. McKenzie, M. Field, B. Haberl, R. Boehler, B. A. Cook, C. de Tomas, I. Suarez-Martinez, N. A. Marks, and J. E. Bradby, Phys. Rev. Lett. **120**, 215701 (2018).

[41] S. Plimpton, J. Chem. Phys. **117**, 1 (1995).

[42] K. Faber, F. Badaczewski, M. Oschatz, G. Mondin, W. Nickel, S. Kaskel, and B. M. Smarsly, J. Phys. Chem. C **118**, 15705 (2014).

[43] S. Osswald, J. Chmiola, and Y. Gogotsi, Carbon **50**, 4880 (2012).

[44] Y. Gogotsi, S. Welz, D. A. Ersoy, and M. J. McNallan, Nature **411**, 283 (2001).

[45] A. Politano and G. Chiarello, Nano Research **8**, 1847 (2015).

[46] M. Long and H. J. Rack, Biomaterials **19**, 1621 (1998).

[47] "MatWeb–The online materials information resources," www.matweb.com; accessed 6 March 2018.

[48] M. Niinomi, Y. Liu, M. Nakai, H. Liu, and H. Li, Regen. Biomater. **3**, 173 (2016).

[49] M. Hendrickson, S. A. Mantri, Y. Ren, T. Alam, V. Soni, B. Gwalani, M. Styles, D. Choudhuri, and R. Banerjee, J. Mat. Sci. **52**, 3062 (2017).

[50] M. Rose, Y. Korenblit, E. Kockrick, L. Borchardt, M. Oschatz, S. Kaskel, and G. Yushin, Small **7**, 1108 (2011).

[51] E. Kockrick, C. Schrage, L. Borchardt, N. Klein, M. Rose, I. Senkovska, and S. Kaskel, Carbon **48**, 1707 (2010).

[52] S.-H. Yeon, P. Reddington, Y. Gogotsi, J. E. Fischer, C. Vakifahmetoglu, and P. Colombo, Carbon **48**, 201 (2010).

[53] A. Turchanin and A. Gölzhäuser, Adv. Mater. **28**, 6075 (2016).

[54] Z. Qin, G. S. Jung, and M. J. Kang, M J Buehler, Sci. Adv. **3**, e1601536 (2017).

SUPPLEMENTARY MATERIAL

Carbide-derived carbons for dense and tunable 3D graphene networks

Carla de Tomas,* Irene Suarez-Martinez, and Nigel A. Marks

Department of Physics and Astronomy, Curtin University, Perth WA 6102, Australia

E-mail: carladetomasandres@curtin.edu.au

Microstructure characterization

Energy minimization using a conjugate gradient scheme is performed prior to all structural analysis. Coordination number of each atom is computed by counting nearest neighbours up to a cut-off of 1.85 Å. In Fig. S1 we show the dependence of sp, sp^2 and sp^3 fractions with density and temperature. Shortest-path ring statistics are calculated using the algorithm of Franzblau,[1] using an in-house code previously used to study amorphous carbon.[2] In Fig. S2 we show the number of rings per atom, i.e pentagons, hexagons, heptagons and octagons.

Calculation of the mechanical properties

To compute the elastic constant tensor for each structure, we first relax the simulation box to zero pressure and minimize the energy. An average minimum of 150,000 iterations were required to fully relax each structure with stopping tolerance criteria of 10^{-14} for the energy and 10^{-16} eV/Å for the forces. Next a small deformation of 10^{-3} is imposed on the system by tilting the box in every direction followed by an energy minimization with the same tolerance
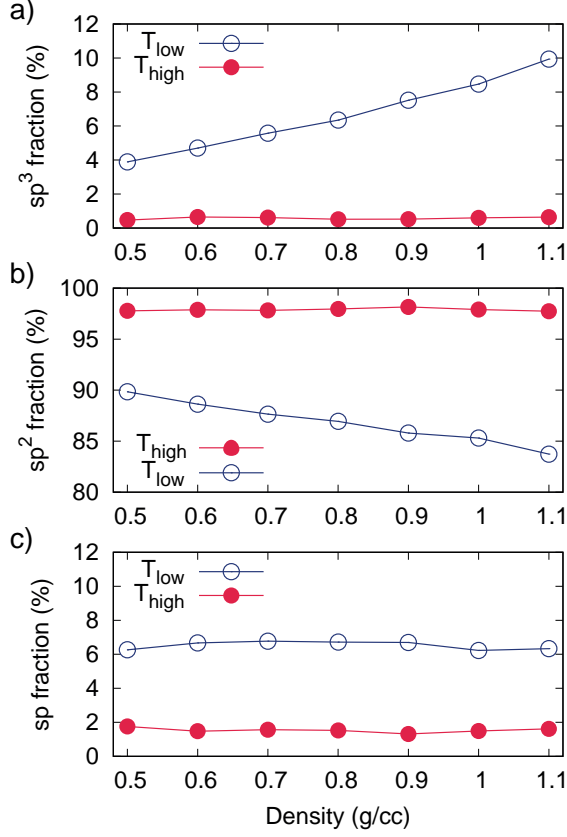
1

Figure S1: Dependence of atomic coordination fractions with density at low and high annealing temperatures. Panel a) shows fraction of sp^3 bonded atoms, b) fraction of sp^2 bonded atoms and c) fraction of sp bonded atoms.

criteria. The corresponding term of the elastic tensor C_{ij} is calculated as the ratio between the stress σ and the strain ϵ in the corresponding direction.[3] The bulk modulus K and the shear modulus G are calculated from the elements of the elastic constant tensor using the Voigt formulas:[3,4]

$$K_{\text{Voigt}} = \frac{1}{9}[C_{11} + C_{22} + C_{33} + 2(C_{12} + C_{13} + C_{23})] \tag{S1}$$

$$
\begin{aligned}
G_{\text{Voigt}} = \frac{1}{15}[&C_{11} + C_{22} + C_{33} + 3(C_{44} + C_{55} + C_{66}) - \\
& - C_{12} - C_{13} - C_{23}]
\end{aligned}
\tag{S2}
$$

The elastic compliance tensor is calculated by inverting the elastic constant tensor. Ac-
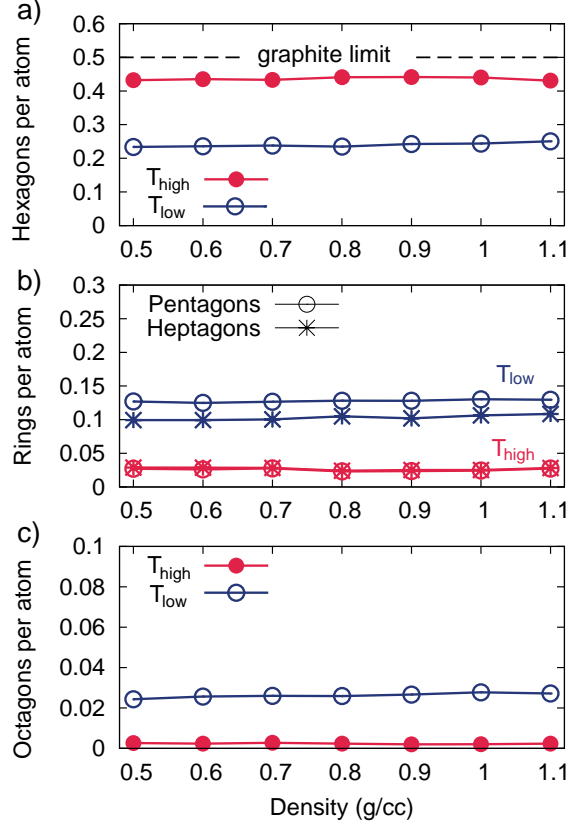
Figure S2: Density dependence of the number of rings per atom for annealing at T_{low} (blue symbols) and T_{high} (red symbols). Panel a) shows number of hexagons per atom, ideal graphite limit of 0.5 hexagons per atom is shown as a dashed line. Panel b) shows the number of pentagons (circles) and heptagons (asterisks). Panel c) shows the number of octagons per atom.

cording to Reuss formula, K and G can be calculated using the components of the compliance tensor S_{ij} as:[3,4]

$$K_{\text{Reuss}} = [S_{11} + S_{22} + S_{33} + 2(S_{12} + S_{13} + S_{23})]^{-1} \tag{S3}$$

$$\begin{aligned} G_{\text{Reuss}} = 15/[&4(S_{11} + S_{22} + S_{33} - S_{12} - S_{13} - S_{23}) + \\ &+ 3(S_{44} + S_{55} + S_{66})] \end{aligned} \tag{S4}$$

3

The Hill formula is defined as the average between the Voigt and the Reuss values:[3,4]

$$K_{\text{Hill}} = \frac{1}{2}(K_{\text{Voigt}} + K_{\text{Reuss}}) \tag{S5}$$

$$G_{\text{Hill}} = \frac{1}{2}(G_{\text{Voigt}} + G_{\text{Reuss}}) \tag{S6}$$

The Young's moduli in each direction is calculated from the elastic compliance:[3,4]

$$Y_x = S_{11}^{-1} \tag{S7}$$

$$Y_y = S_{22}^{-1} \tag{S8}$$

$$Y_z = S_{33}^{-1} \tag{S9}$$

The average Young's modulus is $Y = \frac{1}{3}(Y_x + Y_y + Y_z)$.

Sensitivity analysis

The initialization step of the simulations involves a velocity distribution created using random values, and hence the final structure is not unique. This non-uniqueness, which is intrinsic to molecular dynamics and monte carlo methods, raises the possibility that the structural and mechanical properties might vary if the simulation were repeated using a different random seed. We considered running a suite of additional simulations for each temperature and density combination to extract error bars by brute force, but this would have been impractical, requiring around 1 million cpu-hours of supercomputing time. Instead, we performed two types of sensitivity analysis on the mechanical properties.

The quickest approach involves a least-squares fitting procedure applied to the elastic constant data in Fig. 2 of the main manuscript. Assuming a quadratic dependence on density, the residual-sum-of-squares (RSS) becomes the estimator for the standard deviation
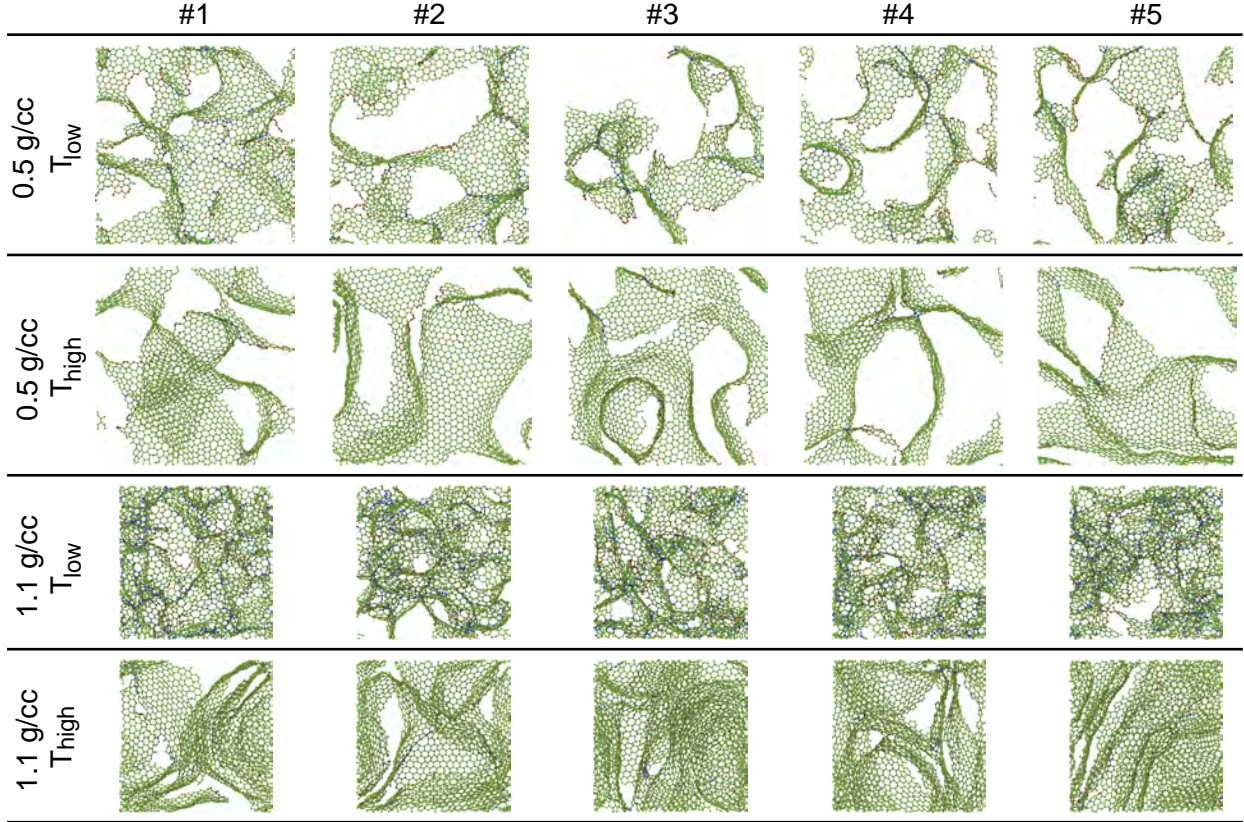
Figure S3: Sensitivity analysis of simulated CDC structures (2 nm cross-sections) obtained by annealing at T_{high}, and T_{low} at both 0.5 and 1.1 g/cc. Five structures are generated for each combination of temperature and density. Structures contain 8,788 atoms. Red, green and blue spheres denote sp, sp^2 and sp^3 bonded atoms, respectively.

of the underlying scatter (which is presumed to be normally distributed). This analysis yields an estimate of 0.3 GPa for the standard-deviation of the T_{low} structures, and 2 GPa for the T_{high} structures. Due to the small sample size of seven points, both of these estimates have an uncertainty of around a factor of two. For the Poisson ratio, the same analysis yields standard-deviation estimates of 0.003 and 0.03 for the T_{low} and T_{high} structures, respectively.

The second approach addresses the question of non-uniqueness by explicitly calculating the mean, standard-deviation and standard-error-in-the-mean of coordination fractions, ring statistics and mechanical properties for 20 additional structures. The additional simulations used different random number seeds to generate five CDC structures at (i) T_{low} and T_{high}, and (ii) the lowest and highest densities. To reduce the computational cost, these additional

20 simulations were performed in a smaller simulation cell (65% of the box length, compared to the original structures), reducing the number of atoms from 32,000 to 8,788. In every other respect the methodology was identical to that for the large structures reported in the main body of the text.

Cross-sectional slices of the 20 structures are shown in Fig. S3, showing the five different structures created for each density and temperature combination. Within each set of simulations (i.e. a row in Fig. S3) there are obvious visual differences specific to the size of pores, number of stacked layers, orientation, etc. These variations arise from the randomized initial conditions and highlight the non-uniqueness of the method. Despite these differences, the five structures in each row share many common characteristics and furthermore, closely resemble the corresponding large structures in Fig. 1 of the main manuscript.

A statistical analysis of the 20 structures is provided in Tables S1 to S4, reporting coordination fractions, ring statistics (expressed as number of rings per atom) and elastic properties (using Hill values). For comparison, we show the values for the corresponding large structure at the bottom of each table. The coordination fractions and ring statistics show little variability across the amongst the five structures, and are close to the corresponding large structure. A similar situation applies for the elastic constants, albeit with slightly higher variability. The only exception is the highly anisotropic and layered T_{high} structure at 1.1 g/cc. Even for this structure, the SEM is still only a few GPa, and two of the three elastic constants are very close to those of the large structure. Note that the small box magnifies the effect of anisotropy, as mentioned in the manuscript.

Calculation of the stress-strain curve

To obtain stress-strain curves we apply uniaxial tensile strain along the x-direction. The strain rate is 0.001 ps^{-1} and is applied to the system every 0.02 ps. The simulation is run for 2 ns in the NPT ensemble where a Nosé-Hoover thermostat is used to keep the temperature at

Table S1: Statistical variability analysis at a density of 0.5 g/cc for T_{low}. Coordination fractions, ring statistics and elastic constants are listed for all five small structures. Also shown is the mean, standard deviation (SD) and standard-error-in-the-mean (SEM) for each property. The final line shows the properties of the corresponding large structure from the main body of the manuscript.

structure	sp (%)	sp^2 (%)	sp^3 (%)	N_5	N_6	N_7	N_8	Y (GPa)	K (GPa)	G (GPa)	σ
# 1	6.50	90.02	3.40	0.127	0.233	0.096	0.024	14.09	10.48	11.30	0.258
# 2	6.17	90.51	3.30	0.129	0.229	0.097	0.026	19.70	13.43	13.27	0.256
# 3	5.66	90.33	3.96	0.127	0.238	0.102	0.023	18.59	10.87	12.06	0.219
# 4	6.44	89.92	3.60	0.130	0.226	0.101	0.025	15.84	10.02	11.21	0.240
# 5	6.90	89.21	3.82	0.124	0.239	0.095	0.023	16.51	8.93	9.87	0.210
Mean	6.33	90.00	3.62	0.127	0.233	0.098	0.024	16.95	10.75	11.54	0.237
SD	0.41	0.45	0.25	0.002	0.005	0.003	0.001	1.99	1.49	1.12	0.019
SEM	0.21	0.22	0.12	0.001	0.003	0.001	0.001	1.00	0.75	0.56	0.010
Large	6.32	89.80	3.89	0.127	0.234	0.099	0.024	17.80	11.98	12.17	0.250

Table S2: Statistical variability analysis at a density of 0.5 g/cc for T_{high}. Coordination fractions, ring statistics and elastic constants are listed for all five small structures. Also shown is the mean, standard deviation (SD) and standard-error-in-the-mean (SEM) for each property. The final line shows the properties of the corresponding large structure from the main body of the manuscript.

structure	sp (%)	sp^2 (%)	sp^3 (%)	N_5	N_6	N_7	N_8	Y (GPa)	K (GPa)	G (GPa)	σ
# 1	2.01	96.83	0.48	0.026	0.429	0.030	0.001	16.33	10.03	12.91	0.224
# 2	2.29	96.32	0.47	0.023	0.436	0.025	0.001	15.72	8.19	10.69	0.179
# 3	2.57	96.03	0.44	0.030	0.419	0.031	0.002	9.66	5.30	7.98	0.176
# 4	2.09	96.68	0.41	0.027	0.431	0.027	0.003	11.96	6.13	8.04	0.195
# 5	1.79	96.50	0.32	0.026	0.430	0.029	0.001	8.99	5.09	7.56	0.140
Mean	2.15	96.47	0.42	0.026	0.429	0.028	0.002	12.53	6.95	9.44	0.183
SD	0.26	0.28	0.06	0.002	0.005	0.002	0.001	3.02	1.89	2.06	0.027
SEM	0.13	0.14	0.03	0.001	0.003	0.001	0.000	1.51	0.95	1.03	0.014
Large	2.57	96.97	0.47	0.027	0.428	0.029	0.003	10.93	4.85	7.64	0.153

Table S3: Statistical variability analysis at a density of 1.1 g/cc for T_{low}. Coordination fractions, ring statistics and elastic constants are listed for all five small structures. Also shown is the mean, standard deviation (SD) and standard-error-in-the-mean (SEM) for each property. The final line shows the properties of the corresponding large structure from the main body of the manuscript.

structure	sp (%)	sp^2 (%)	sp^3 (%)	N_5	N_6	N_7	N_8	Y (GPa)	K (GPa)	G (GPa)	σ
# 1	6.04	83.71	10.23	0.131	0.252	0.112	0.025	84.02	57.68	57.28	0.257
# 2	6.29	83.72	9.95	0.129	0.252	0.108	0.027	82.85	56.22	56.59	0.255
# 3	5.87	84.43	9.68	0.127	0.255	0.108	0.027	82.38	57.50	56.21	0.262
# 4	5.71	84.71	9.56	0.127	0.254	0.106	0.031	81.19	57.73	56.37	0.265
# 5	5.92	84.50	9.57	0.130	0.249	0.108	0.028	83.58	56.55	56.20	0.255
Mean	5.97	84.21	9.80	0.129	0.252	0.108	0.028	82.81	57.14	56.53	0.259
SD	0.19	0.42	0.26	0.002	0.002	0.002	0.002	0.99	0.63	0.40	0.004
SEM	0.10	0.21	0.13	0.001	0.001	0.001	0.001	0.49	0.31	0.20	0.002
Large	6.35	83.72	9.93	0.130	0.251	0.108	0.027	82.70	57.47	56.06	0.260

Table S4: Statistical variability analysis at a density of 1.1 g/cc for T_{high}. Coordination fractions, ring statistics and elastic constants are listed for all five small structures. Also shown is the mean, standard deviation (SD) and standard-error-in-the-mean (SEM) for each property. The final line shows the properties of the corresponding large structure from the main body of the manuscript.

structure	sp (%)	sp^2 (%)	sp^3 (%)	N_5	N_6	N_7	N_8	Y (GPa)	K_{Hill} (GPa)	G_{Hill} (GPa)	σ
# 1	1.98	97.21	0.59	0.024	0.435	0.023	0.002	28.98	21.26	28.82	0.269
# 2	1.79	97.41	0.44	0.026	0.434	0.024	0.002	15.76	11.34	18.73	0.200
# 3	1.93	97.29	0.55	0.025	0.435	0.024	0.002	14.78	8.41	14.92	0.192
# 4	2.21	97.09	0.60	0.025	0.431	0.026	0.001	34.62	20.89	28.41	0.170
# 5	2.08	97.27	0.47	0.028	0.424	0.029	0.002	22.91	14.35	21.78	0.149
Mean	2.00	97.25	0.53	0.026	0.432	0.025	0.002	23.41	15.25	22.53	0.196
SD	0.14	0.10	0.06	0.001	0.004	0.002	0.000	7.62	5.11	5.42	0.041
SEM	0.07	0.05	0.03	0.001	0.002	0.001	0.000	3.81	2.56	2.71	0.020
Large	1.76	97.60	0.64	0.027	0.430	0.028	0.002	35.37	18.62	26.96	0.195

300 K and the pressure at zero in the y and z-directions, so the system responds dynamically to the applied strain. In Fig. S4 we show the curves for all densities and the two annealing temperatures. The ultimate tensile strength is obtained from the point of maximum stress in the stress-strain curve. The yield stress is obtained from the last point in the linear regime. The Young's modulus in the tensile direction Y_x can be calculated from the slope of the stress-strain curve in the linear regime. This represents an alternative method to Eq. S7. In Fig. S5 we compare both methods for the T_{low} and T_{high} structures. The structures at T_{low} show a good correlation between both methods at all densities, with differences between 5 and 15%. The structures at T_{high} show a good correlation, between 10 and 20%, for densities

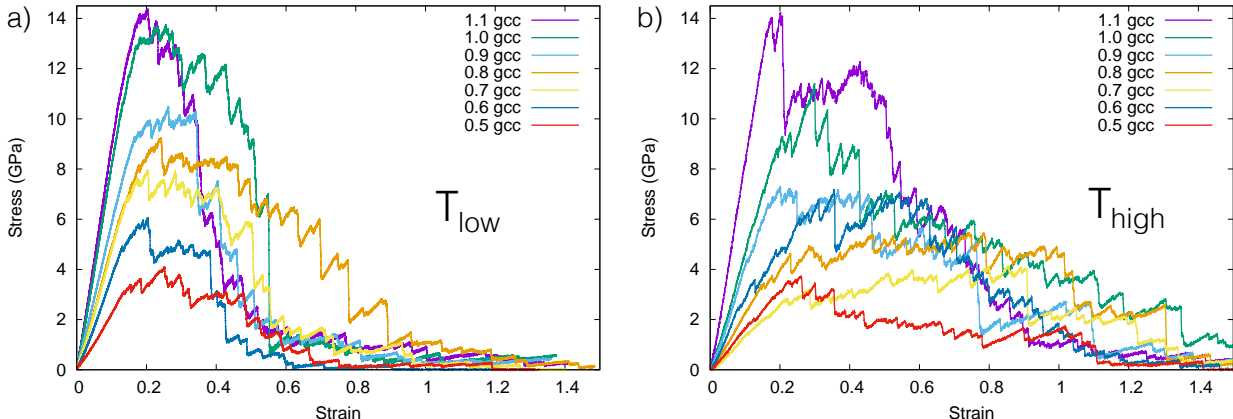Figure S4: Stress-strain curves for all the CDC structures annealed at a) T_{low}, and b) T_{high}.

up to 0.9 g/cc. The only significant difference, around 30%, occur for the 1 and 1.1 g/cc. Good overall agreement between both methods reinforces the robustness of the calculations.
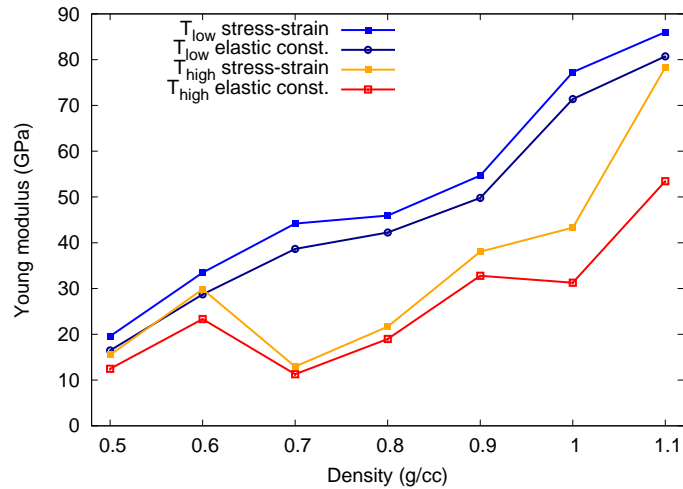

Figure S5: Young's modulus as a function of density and temperature. For each annealing temperature, results obtained from the stress-strain curve are plotted against results derived from the elastic constant tensor (blue squares and open circles respectively, for T_{low}; orange squares and red open squares, respectively, for T_{high}).

References

(1) Franzblau, D. S. Computation of ring statistics for network models of solids. *Phys. Rev. B* **1991**, *44*, 4925–4930.

(2) Marks, N. A.; Cooper, N. C.; McKenzie, D. R.; McCulloch, D. G.; Bath, P.; Russo, S. P. Comparison of density-functional, tight-binding, and empirical methods for the simulation of amorphous carbon. *Phys. Rev. B* **2002**, *65*, 075411.

(3) Caruta, B. M. *Ceramics and composite materials: new research*; Nova publishers, 2006.

(4) Levy, M.; Bass, H. E.; Stern, R. R.; Keppens, V. *Handbook of elastic properties of solids, liquids and gasses*; Academic Press, 2001.